

Efficiency Optimization of Four-Switch Buck-Boost Converter Using Frequency-domain Analysis

Guanqun Qiu, *Student Member, IEEE*, Vinod Khadkikar, *Fellow, IEEE*, Bashar Zahawi, *Senior Member, IEEE*, and Jianqun Liao, *Member, IEEE*

Abstract- A bidirectional four-switch buck-boost (FSBB) converter offers more control variables than a classical buck-boost converter and can thus achieve higher power efficiencies through appropriate control. Traditionally, efficiency is optimized by reducing the inductor current RMS value (or conduction loss) obtained through time-domain analysis. However, it is extremely difficult to use this time-domain approach to include converter switching losses in the efficiency optimization for all possible modulation modes. To solve this problem, this article proposes a frequency-domain analysis to estimate switching losses and establish a comprehensive loss model that allows for the efficiency to be optimized using a Gaussian quantum-behaved particle swarm optimization (GQPSO) algorithm. The switching frequency is then used as an additional optimization variable to improve the efficiency over a much wider range of operating conditions. The proposed method is verified experimentally, using 600W and 1500W rated laboratory prototypes, and compared with existing methods. Results demonstrate the effectiveness of the proposed technique in increasing converter efficiency over the whole range of load conditions.

Index Terms- Four-switch buck-boost, FSBB, frequency-domain, Gaussian quantum-behaved particle swarm optimization, GQPSO, PSO, ZVS, DC-DC converter

I. INTRODUCTION

Bidirectional buck-boost converters have been widely adopted in electrical vehicles [1]-[4], DC microgrids [5], energy storage systems [6], and so on. Four-switch buck-boost (FSBB) converter (as shown in Fig. 1) is a typical bidirectional buck-boost converter that enjoys a wide range of operating input and output voltages and is gaining in popularity at an increasing rate in aforementioned applications.

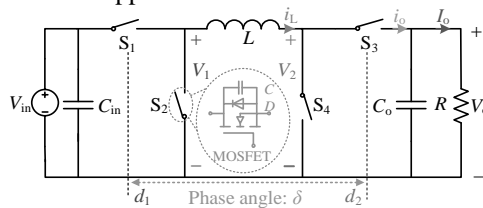


Fig. 1 Four-switch buck-boost (FSBB) converter.

In FSBB converters, the duty cycle d_1 of switch pair S_1 - S_2 , the duty cycle d_2 of switch pair S_3 - S_4 and the phase angle δ between d_1 and d_2 can provide diverse modulation modes for the same loading condition. If these control parameters are

Manuscript received February 01, 2024; revised April 30, 2024; accepted July 08, 2024. This work was supported by the ASPIRE, the technology program management pillar of Abu Dhabi's Advanced Technology Research Council (ATRC) via the ASPIRE "Virtual Research Institute (VRI)" under Grant VRI20-07. (Corresponding author: Vinod Khadkikar)

Guanqun Qiu, Vinod Khadkikar, and Bashar Zahawi are with the Advanced Power and Energy Centre (APEC), Department of Electrical Engineering, Khalifa University, PO Box 127788, Abu Dhabi, UAE (email: 100061995@ku.ac.ae; vinod.khadkikar@ku.ac.ae; bashar.zahawi@ku.ac.ae).

Jianqun Liao is with the School of Electrical Engineering, Sichuan University, Chengdu 610065, China (e-mail: jqunliao@scu.edu.cn).

unsuitable, a large inductor current that leads to a reduction in power efficiency will be generated. Therefore, researchers have proposed different control methods to reduce the inductor current. These control methods can be classified depending on the number of modulation modes used in the process.

The first category is characterized by the use of one modulation mode [7]-[15]. In [7] it is suggested that the duty cycle d_1 or d_2 is made equal to 1. However, the paper did not consider zero-voltage switching (ZVS) as a means of reducing power losses. ZVS was introduced in [2] to increase the converter power density with one modulation mode. In addition, several improved methods were later developed in [8]-[15] by using various optimization techniques to further reduce inductor current and improve efficiency. In [8], the power efficiency is optimized for different operating conditions by limiting the control parameter range to reduce the peak and RMS inductor current. In [9] and [10], the minimum inductor current RMS value is calculated by taking the derivative of its expression. Similarly, the derivative of conduction loss and inductor loss are taken to find the minimum loss in [11]. Besides, the relationship between minimum RMS value and ZVS was derived for reducing inductor power loss [12]. Feiming *et al.* [13] used a monotonically increasing function to determine the control variables to reduce the inductor current. In [14], a multi-frequency ZVS modulation scheme was developed to reduce the inductor current RMS value. The minimum peak-to-peak inductor current was found through the Lagrange multipliers algorithm in [15]. In all the abovementioned works, the optimal inductor current RMS value is determined for only one modulation mode. As a result, these methods provide a local optimum inductor current, instead of a global optimum.

To overcome this issue, authors in [16]-[18] developed multiple modulation modes control methods (the second category in our classification). Ren *et al.* [16] developed a two-edge modulation mode that can reduce the inductor current RMS value. A hybrid buck-boost feedforward technique is suggested in [17] to achieve a fast dynamic response while minimizing the conduction loss. Compared to the methods presented in [7]-[15], the light load efficiency is closer to the peak efficiency, i.e., the use of multiple modulation modes (for different loading conditions), can successfully improve converter efficiency. In [18], a Lagrange Multiplier-based method is used to optimize about ten different modulation modes. However, these calculations and derivation are difficult due to the very complex inductor current expressions, requiring the use of mathematical software.

All the above papers (with the exception of [14]) ignore the fact that the switching frequency can be employed as an additional control variable in the optimization process. In [14], multiple switching frequencies are used to reduce the inductor current RMS value (conduction loss). While higher switching frequencies reduce the inductor current RMS value, switching losses will also increase. The tradeoff between switching losses

and conduction losses is not considered, resulting in an inability to determine the total loss reduction. Additionally, the inductor current is optimized for only one modulation mode. Because of these significant drawbacks, the efficiency optimization is not the global optimal value. Note that switching loss was not included in the optimizing process in these studies [7]–[18].

In summary, in the existing literature, the switching loss is not included in the efficiency optimization of FSBB converters. Moreover, none of the published papers have taken into account all possible converter modulation modes in the optimization process to find the global optimum. To fill these gaps, this paper makes the following main contributions:

1) A generalized frequency-domain expression for inductor current RMS value is derived. Compared with time-domain expressions, the frequency-domain expression can represent all possible modulation modes with one expression, ensuring that all modulation modes are included in the optimization process.

2) Extending the existing three-degree-of-freedom FSBB converter control method to four degrees of freedom over the entire load range, thereby adding the switching loss as a parameter in the optimization process. Results show that a tradeoff between switching loss and conduction loss can significantly improve the converter efficiency compared with existing methods.

II. Derivation of Inductor Current Formula

A. Derivation of Inductor Current Formula

Fig. 1 shows a typical FSBB topology. V_{in} and V_o are input and output voltage, respectively. V_1 and V_2 are the inductor left and right terminal voltages, respectively. Switch pairs S_1 – S_2 and S_3 – S_4 are controlled complementarily. Each switch pair offers one control variable through its duty cycle, d_1 for S_1 – S_2 and d_2 for S_3 – S_4 . The phase angle δ between the duty cycle d_1 and d_2 provides a third control variable and switching frequency f_s (or switching period T_s) can be the fourth control variable. The four control variables determine the magnitude of the inductor current RMS value (conduction loss). This is derived from frequency-domain analysis in this paper. Specifically, the inductor current is represented by the composition of a series of sinusoidal harmonics with the Fourier method. The derivation process of inductor current expression is as follows.

Since the FSBB converter is a PWM modulation converter, expressions such as inductor voltage and current can be derived from the PWM signal. In addition, the switching loss estimation requires a gate drive PWM signal to identify the switching instant current. The four FSBB gate drive signals can be expressed using frequency-domain expression as,

$$\begin{cases} G_{S1}(t) = d_1' + 2d_1' \sum_{n=1}^{\infty} \frac{\sin(n\omega d_1' T_s/2)}{n\omega d_1' T_s/2} \cos(n\omega t - n(d_1' + 2d_D)\pi) \\ G_{S2}(t) = d_1'' + 2d_1'' \sum_{n=1}^{\infty} \frac{\sin(n\omega d_1'' T_s/2)}{n\omega d_1'' T_s/2} \cos(n\omega t + nd_1''\pi) \\ G_{S3}(t) = d_2' + 2d_2' \sum_{n=1}^{\infty} \frac{\sin(n\omega d_2' T_s/2)}{n\omega d_2' T_s/2} \cos(n\omega t - n(d_2' + 2\delta + 2d_D)\pi) \\ G_{S4}(t) = d_2'' + 2d_2'' \sum_{n=1}^{\infty} \frac{\sin(n\omega d_2'' T_s/2)}{n\omega d_2'' T_s/2} \cos(n\omega t - n(2\delta - d_2'')\pi) \\ V_o/V_{in} = d_1/d_2, d_D = T_D/T_s, d_1' = d_1 - d_D, d_2' = d_2 - d_D \\ d_1'' = 1 - d_1 - d_D, d_2'' = 1 - d_2 - d_D, \omega = 2\pi/T_s, f_s = 1/T_s \end{cases} \quad (1)$$

where, $G_{S1}(t)$, $G_{S2}(t)$, $G_{S3}(t)$ and $G_{S4}(t)$ are gate drive PWM signals of switches S_1 , S_2 , S_3 and S_4 , respectively. T_D is the

deadtime, d_D is the deadtime duty cycle, d_1' and d_2' are the duty cycles of the left-side and right-side half-bridge without deadtime, respectively. z is the number of harmonics.

The inductor voltage $v_L(t)$ can also be derived based on the gate drive PWM signal. It can be expressed as,

$$v_L(t) = V_{in} \cdot G_{S1}(t) - V_o \cdot G_{S3}(t) \quad (2)$$

The inductor current is then given by,

$$i_L(t) = I_{bias} + i_{ripple}(t) = I_{bias} + v_L(t)/L \quad (3)$$

where, $i_{ripple}(t)$ is the ripple current given by $v_L(t)/L$ and I_{bias} is a DC bias component added to ensure the accuracy of the inductor current, since the actual inductor current includes DC bias, but the ripple current $i_{ripple}(t)$ does not.

The ripple current $i_{ripple}(t)$ in (3) can also be derived using a frequency-domain expression, i.e.,

$$\begin{aligned} i_{ripple}(t) &= v_L(n\omega t + \pi/2)/(n\omega L) \\ &= \sum_{n=1}^z \left[\frac{V_{in}d_1' - V_o d_2'}{zn\omega L} + \frac{\sqrt{A^2 + B^2}}{n\omega L} \sin\left(n\omega t + \arctan\frac{B}{A}\right) \right] \end{aligned} \quad (4)$$

where,

$$\begin{aligned} A &= 2V_{in}d_1' \text{sinc}(n\omega d_1' T_s/2) \sin(n(d_1' + 2d_D)\pi + \pi/2) \\ &\quad - 2V_o d_2' \text{sinc}(n\omega d_2' T_s/2) \sin(n(d_2' + 2(\delta + d_D))\pi + \pi/2) \\ B &= 2V_{in}d_1' \text{sinc}(n\omega d_1' T_s/2) \cos(n(d_1' + 2d_D)\pi + \pi/2) \\ &\quad - 2V_o d_2' \text{sinc}(n\omega d_2' T_s/2) \cos(n(d_2' + 2(\delta + d_D))\pi + \pi/2) \end{aligned}$$

The expression for the inductor ripple current RMS value can be determined from (5) as,

$$I_{ripple,rms} = \sqrt{\sum_{n=1}^z \left(\frac{V_{in}d_1' - V_o d_2'}{zn\omega L} \right)^2 + \sum_{n=1}^z \left(\frac{\sqrt{A^2 + B^2}}{\sqrt{2}n\omega L} \right)^2} \quad (5)$$

The inductor current provides the instantaneous current to the output capacitor when the switch S_3 open (during $d_2' T_s$). Hence, the average output current, I_o , is given by,

$$\begin{aligned} I_o &= \frac{1}{T_s} \int_{\delta T_s}^{(\delta + d_2') T_s} i_L(t) dt = d_2' \left(I_{bias} + \sum_{n=1}^z \frac{V_{in}d_1' - V_o d_2'}{zn\omega L} \right) \\ &\quad + \sum_{n=1}^z \frac{\sqrt{A^2 + B^2}}{n^2 \omega^2 L T_s} \left[\cos(n\omega \delta T_s + \arctan(B/A)) - \cos(n\omega(\delta + d_2') T_s + \arctan(B/A)) \right] \end{aligned} \quad (6)$$

The optimization process is carried out for a given output current value. Therefore, the analytical expression for the DC bias current I_{bias} can be obtained by rearranging (6),

$$\begin{aligned} I_{bias} &= \frac{1}{d_2'} \left\{ I_o - \sum_{n=1}^z \frac{\sqrt{A^2 + B^2}}{d_2' n^2 \omega^2 L T_s} \left[\cos(n\omega \delta T_s + \arctan(B/A)) - \cos(n\omega(\delta + d_2') T_s + \arctan(B/A)) \right] \right\} \\ &\quad - \sum_{n=1}^z (V_{in}d_1' - V_o d_2')/(zn\omega L) \end{aligned} \quad (7)$$

Combining (4) and (7), the complete inductor current frequency-domain expression can be written as,

$$\begin{aligned} i_L(t) &= \frac{1}{d_2'} \left\{ I_o - \sum_{n=1}^z \frac{\sqrt{A^2 + B^2}}{d_2' n^2 \omega^2 L T_s} \left[\cos(n\omega \delta T_s + \arctan(B/A)) - \cos(n\omega(\delta + d_2') T_s + \arctan(B/A)) \right] \right\} \\ &\quad - \sum_{n=1}^z \frac{V_{in}d_1' - V_o d_2'}{zn\omega L} + \sum_{n=1}^z \left[\frac{V_{in}d_1' - V_o d_2'}{zn\omega L} + \frac{\sqrt{A^2 + B^2}}{n\omega L} \sin\left(n\omega t + \arctan\frac{B}{A}\right) \right] \end{aligned} \quad (8)$$

Eq. (8) provides a general expression that can represent all possible modulation modes for the FSBB converter. This means

that the inductor current expression does not need to be derived separately for each modulation mode, which significantly simplifies the optimization process since FSBB converters have at least ten different modulation modes from [7] and [18].

The RMS value of the inductor current $I_{L,rms}$ (needed for power loss calculations) can now be expressed as,

$$I_{L,rms} = \sqrt{I_{bias}^2 + I_{ripple,rms}^2} \quad (9)$$

B. Accuracy of Inductor Current Formula

The accuracy of equations (8) and (9) was tested by assessing the influence of the number of sinusoidal harmonics used to compose the inductor current waveform, and also by comparing the calculation results with simulation results. Fig. 2 shows example waveforms of the gate drive PWM signals, inductor terminal voltages (v_1 and v_2) and inductor current with different numbers of sinusoidal harmonics. It can be seen that the gate drive PWM signals and the profile of inductor terminal voltages improve substantially when the number of harmonics increases. The number of harmonics is set to 200 in this study. It can be seen that the calculated waveforms and simulations waveforms are extremely similar, as demonstrated in Fig. 3. In addition, there was only a 0.63% difference between the simulated RMS current (3.188A) and the calculated RMS current (3.168A). To further verify the accuracy of the RMS current expression, comparisons were carried out between simulated and calculated values under 50 different operating conditions, as shown in Fig. 4. The maximum error was only 1.25% (with an average value of 0.65%), verifying the accuracy of the derived formula.

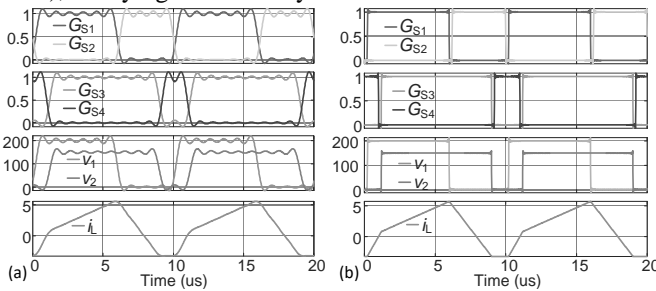


Fig. 2 Example waveforms of gate driver signals, inductor terminal voltages (v_1 and v_2) and inductor current with different number of harmonics z . (a) $z=10$. (b) $z=200$.

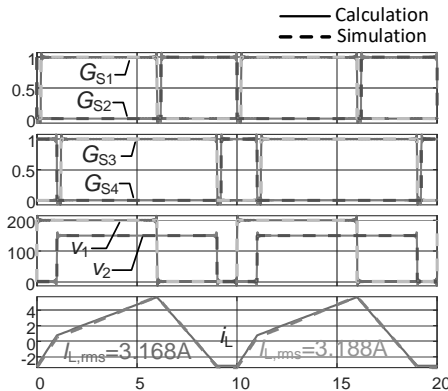


Fig. 3 Comparison of calculated and simulated waveforms with $V_{in}=200V$, $V_o=150V$, $\delta=0.1$, $d_2=0.8$, $d_1=0.6$, and $I_o=2A$.

C. Frequency-domain Expressions vs Time-domain Expressions

Table I shows the comparison between the frequency-domain and the time-domain analysis approach. When using the time-domain (or pieces-wise) method to derive the inductor current RMS value expression, the time interval of each pieces-wise inductor current must be known first. The different modulation

modes are classified according to these different piece-wise time intervals, causing different modulation modes to have different inductor current RMS value expressions. These expressions are so complex that software must be used to derive them, otherwise, the accuracy is hard to guarantee [18]. A literature survey revealed at least 19 different modulations for the FSBB converter, meaning at least 19 different inductor current RMS value expressions may be required. It is also very difficult to confirm whether these 19 modulation modes are exhaustive, presenting one of the major drawbacks of the time-domain approach. What's more, 19 different inductor current RMS value expressions imply 19 different switching loss expressions and at least 19 runs of the GQPSO algorithm to obtain the optimal result for each modulation mode. Comparing all these results is necessary to compute the global optimum. This is a very complex task requiring great effort.

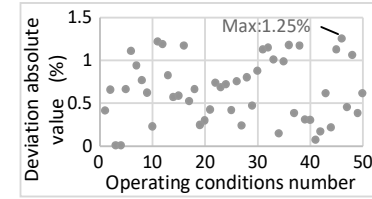


Fig. 4 RMS current deviation between simulation and calculation for 50 different operating conditions (0.65% average deviation).

In contrast, the frequency-domain method can represent the inductor current RMS value for all possible modulation modes by only one expression. This is because the frequency-domain analysis is not constrained by piece-wise time intervals. The frequency domain expression is derived from the PWM signal by hand in a much simpler process than the corresponding time-domain expressions. The estimation of the switching losses is represented by only one expression and the control variables can be varied over their full range in the optimization process meaning that one run of the GQPSO algorithm is sufficient to give the global optimum accounting for all possible modulation modes.

TABLE I

FREQUENCY-DOMAIN EXPRESSIONS VS TIME-DOMAIN EXPRESSIONS

	Frequency-domain	Time-domain
Number of inductor current RMS value formulas	1	>19
Derivation approach	By hand	By Mathematical software
Number of switching loss expressions	1	>19
Number of GQPSO runs	1	>19
Complexity level	Low	High
Number of optimized modulation modes	All	Partial

III. FSBB CONVERTER POWER LOSS MODEL

The converter power loss is comprised of the following main components: conduction loss, inductor core loss, MOSFET switching loss, and the MOSFET body diode loss.

A. Conduction Loss

The conduction loss (P_{con}) consists of four parts: MOSFET conduction losses (P_{mos}), capacitor conduction losses (P_{cap}), the loss in the inductor winding parasitic resistance (P_{LR}), and the losses in the connecting cables/wires (P_{wire}).

Four MOSFETs of the same type are used in this converter. Based on the gate drive PWM signal expressions and the

inductor current expression, each MOSFET conduction current can be calculated as $i_L(t)G_{Sx}(t)$. Including the relationship between MOSFET on-state resistance R_{DSon} and the junction temperature T_j , the conduction loss of the four MOSFETs can be expressed as,

$$P_{mos} = I_{S1,rms}^2 R_{DSon}(T_{j,1}) + I_{S2,rms}^2 R_{DSon}(T_{j,2}) + I_{S3,rms}^2 R_{DSon}(T_{j,3}) + I_{S4,rms}^2 R_{DSon}(T_{j,4}) \quad (10)$$

where

$$\begin{cases} I_{S1,rms} = \sqrt{\int_0^{T_s} (i_L(t)G_{S1}(t))^2 dt / T_s}, & I_{S2,rms} = \sqrt{\int_0^{T_s} (i_L(t)G_{S2}(t))^2 dt / T_s} \\ I_{S3,rms} = \sqrt{\int_0^{T_s} (i_L(t)G_{S3}(t))^2 dt / T_s}, & I_{S4,rms} = \sqrt{\int_0^{T_s} (i_L(t)G_{S4}(t))^2 dt / T_s} \end{cases}$$

According to the SPICE model of the MOSFET from the manufacturer, the relationship between R_{DSon} and the junction temperature T_j is shown in Fig. 5 and can be expressed as

$$R_{DSon}(T_j) = c_1 T_j^3 + c_2 T_j^2 + c_3 T_j + c_4 \quad (11)$$

where, c_1 , c_2 , c_3 and c_4 are constant coefficients. The junction temperature can be estimated by

$$T_j = T_h(P_o) + (R_{th,ja} + R_{pad})P_{diss} \quad (12)$$

where, $T_h(P_o)$ is the temperature of the point close to the MOSFET case and the heat sink, and it is a function of the output power P_o that can be determined experimentally. $R_{th,ja}$ is the thermal resistance from junction to ambient, which can be found in the MOSFET datasheet. R_{pad} is the thermal resistance of the Al_2O_3 thermal pad between the MOSFET case and the heat sink. P_{diss} is the power loss in the MOSFET.

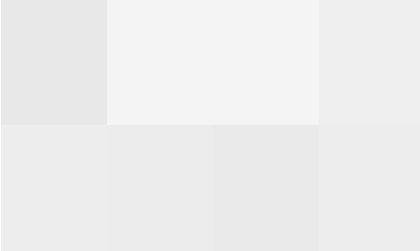


Fig. 5 Relationship between R_{DSon} and the junction temperature T_j .

It is worth noting that the MOSFET junction temperature varies less when the MOSFET losses are small and the effectiveness of the cooling system is high. Under these conditions, $R_{DSon}(T_j)$ can be considered as a constant and equation (10) can be simplified to

$$\begin{aligned} P_{mos} &= (I_{S1,rms}^2 + I_{S2,rms}^2 + I_{S3,rms}^2 + I_{S4,rms}^2) R_{DSon} \\ &= \left(\int_0^{T_s} (i_L(t)G_{S1}(t))^2 dt / T_s + \int_0^{T_s} (i_L(t)G_{S2}(t))^2 dt / T_s \right. \\ &\quad \left. + \int_0^{T_s} (i_L(t)G_{S3}(t))^2 dt / T_s + \int_0^{T_s} (i_L(t)G_{S4}(t))^2 dt / T_s \right) R_{dson} \quad (13) \\ &= 2I_{L,rms}^2 R_{dson} \end{aligned}$$

The input capacitor ripple current is equal to the current flowing through S_1 minus the input DC current I_{in} . Similarly, the output capacitor ripple current is equal to the current flowing through S_3 minus the DC output current I_o . The expression for capacitor conduction loss is given by,

$$\begin{cases} P_{cap} = (I_{Cin,rms})^2 R_{cap}(f_s) + (I_{Co,rms})^2 R_{cap}(f_s) \\ I_{Cin,rms} = \sqrt{\int_0^{T_s} (i_L(t)G_{S1}(t) - I_{in})^2 dt / T_s} \\ I_{Co,rms} = \sqrt{\int_0^{T_s} (i_L(t)G_{S3}(t) - I_o)^2 dt / T_s} \end{cases} \quad (14)$$

where, $I_{Cin,rms}$ and $I_{Co,rms}$ are the input and output capacitor RMS currents, respectively. $R_{cap}(f_s)$ is the capacitor equivalent series resistance (ESR) that changes with switching frequency.

The inductor winding parasitic resistor loss is expressed as,

$$P_{LR} = I_{bias}^2 R_{L,dc} + I_{ripple,rms}^2 R_{L,ac}(f_s) \quad (15)$$

where, $R_{L,dc}$ is the winding dc resistance, and $R_{L,ac}(f_s)$ is the equivalent resistance that changes with switching frequency due to the skin effect. The parasitic resistances R_{cap} and $R_{L,ac}$ were measured with an IM3570 impedance analyzer whose accuracy is 0.08%. The results are shown in Fig. 6.

The expression for the loss of the connecting wires is,

$$P_{wire} = I_{in}^2 R_{in} + I_o^2 R_o \quad (16)$$

where, R_{in} and R_o are input and output wire resistances, respectively.

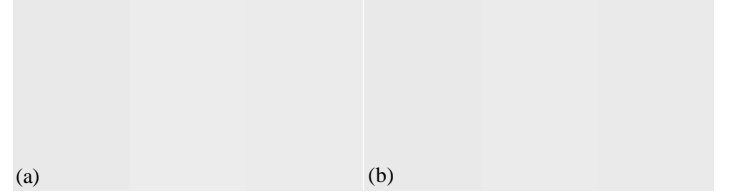


Fig. 6 Parasitic resistances measured using the IM3570 impedance analyzer: (a) R_{cap} and (b) $R_{L,ac}$.

The converter's total conduction loss can be expressed as,

$$P_{con} = P_{mos} + P_{cap} + P_{LR} + P_{wire} \quad (17)$$

B. Inductor Core Loss

The inductor core is PQ26/20-N95 from TDK company. The inductor core loss can be estimated by the expression [19],

$$\begin{cases} P_{core} = V_e \cdot C_m(T_{core}) \cdot f_s^{\alpha(T_{core})} \cdot \hat{B}^{\beta(T_{core})} \\ \hat{B} = L \cdot \max(i_L(t)) / (NA_e) \end{cases} \quad (18)$$

where, P_{core} is the inductor core loss, V_e is the effective core volume, and A_e is the effective cross-sectional area of the core. N is the number of turns in the inductor winding. $C_m(T_{core})$, $\alpha(T_{core})$ and $\beta(T_{core})$ are the Steinmetz coefficients for different core temperatures obtained from the manufacturer.

Analysis of the core loss coefficients given by TDK reveals that when the core temperature can be guaranteed to be lower than 80°C, the core loss remains almost unchanged. In this study, the core loss is small and the inductor is air-cooled (by fan) resulting in the core temperature being much lower than 80°C during actual operation. Equation (11) can then be simplified to

$$\begin{cases} P_{core} = V_e \cdot C_m \cdot f_s^\alpha \cdot \hat{B}^\beta \\ \hat{B} = L \cdot \max(i_L(t)) / (NA_e) \end{cases} \quad (19)$$

C. Switching Loss

With reference to [19], a simple switching loss model based on the MOSFET SPICE model simulations is used to estimate the switching loss. The double pulse circuit was established in LTSPICE software to record the turn-on energy loss $E_{on}(I_{on}, V_{DS})$ and the turn-off energy loss $E_{off}(I_{off}, V_{DS})$ at different values of switching currents and voltages, as shown in Fig. 7. A curve-fitting method was then utilized to obtain suitable expressions for $E_{off}(I_{off}, V_{DS})$ and $E_{on}(I_{on}, V_{DS})$,

$$\begin{cases} E_{off}(I_{off}, V_{DS}) = aI_{off}^3 + bI_{off}^2 + cI_{off} + d \\ E_{on}(I_{on}, V_{DS}) = eI_{on} + f \end{cases} \quad (20)$$

where, a, b, c, d, e , and f are the curve-fitting coefficients. The current at the turn-on and turn-off instants can be found from the calculated gate drive signal and inductor current waveforms (those shown in Fig. 3 as an example).

A simple switching loss expression can be derived as,

$$P_{sw} = 10^{-6} f_s \left(E_{off}(I_{off}, V_{DS})(S_1, S_2, S_3, S_4) + E_{on}(I_{on}, V_{DS})(S_1, S_2, S_3, S_4) \right) \quad (21)$$

D. Switching Loss Special Conditions

Two special cases need to be considered when calculating switching loss.

1) ZVS

To achieve ZVS, a minimum inductor current is required to discharge the MOSFET output parasitic capacitors C_{oss} . This can be determined as [13],

$$|I_{zvs_min}| \geq 2 \max(V_{in}, V_o) C_{oss} / T_D \quad (22)$$

To achieve ZVS, S_2 and S_3 should turn-on when $i_L(t) \geq |I_{zvs_min}|$, and S_1 and S_4 should turn-on when $i_L(t) \leq -|I_{zvs_min}|$ [7].

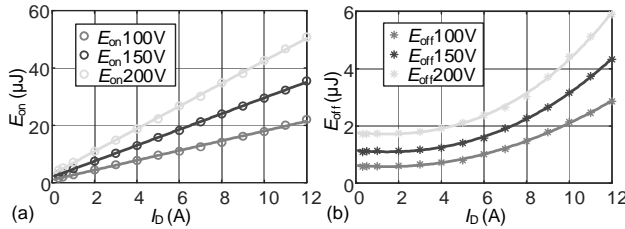


Fig. 7 Turn-on energy losses $E_{on}(I_{on}, V_{DS})$ and turn-off energy losses $E_{off}(I_{off}, V_{DS})$ data from LTSPICE software with curve-fitting.

2) The duty cycle equals to one

A duty cycle equal to one is a special modulation mode [7] in the FSBB converter. S_1 is on, S_2 is off, S_3 and S_4 works at high frequency when the duty cycle $d_1=1$, and $d_2<1$. The remaining circuit components make up a boost converter under this condition, as shown in Fig. 8 (a). Similarly, S_3 is on, S_4 is off, S_1 and S_2 works at high frequency when the duty cycle $d_2=1$, and $d_1<1$. The remaining circuit components make up a buck circuit, as shown in Fig. 8 (b).

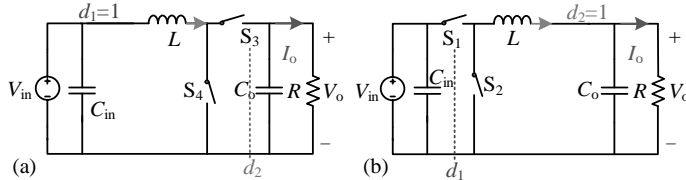


Fig. 8 (a) Boost mode: duty cycle $d_1=1, d_2<1$. (b) Buck mode: duty cycle $d_2=1, d_1<1$.

When $d_1=1$, the turn-on/off loss of the switch pair S_1 - S_2 and phase angle δ are zero. The remaining control variables are the duty cycle d_2 and the switching frequency f_s . Similarly, the turn-on/off loss of the switch pair S_3 - S_4 and phase angle δ is also zero when the duty cycle $d_2=1$. The only remaining control variables are the duty cycle d_1 and the switching frequency f_s .

E. MOSFET Body Diode Loss

The power loss of the MOSFET body diode P_{diode} can be divided into two parts: the conduction loss $P_{D,con}$ and the reverse recovery loss $P_{D,r}$. The body diode conducts during deadtime, but for a shorter period than the deadtime because it begins conduction after the output capacitor C_{oss} is fully discharged. $P_{D,con}$ can be expressed as,

$$\begin{cases} P_{D,con} = V_F(I_F) |I_{zvs}| (T_D - T_{dis}) / T_s \\ T_{dis} = V_{DS} C_{oss} / |I_{zvs}|, V_{DS} = V_{in} \text{ or } V_o \end{cases} \quad (23)$$

where, $V_F(I_F)$ is the forward voltage that changes with the conduction current, V_{DS} is the voltage between the drain and the source of the MOSFET, T_{dis} is the discharging time of C_{oss} .

The diode reverse recovery loss $P_{D,r}$ can be expressed as,

$$P_{D,r} = V_{DS} Q_{rr}(I_{off}, V_{DS}) f_s \quad (24)$$

where, $Q_{rr}(I_{off}, V_{DS})$ is the reverse recovery charge changes with the turn-off voltage and current.

Note that $V_F(I_F)$ and $Q_{rr}(I_{off}, V_{DS})$ can also be obtained by the SPICE model provided by the manufacturer through LTSPICE software. The curve-fitting for $V_F(I_F)$ and $Q_{rr}(I_{off}, V_{DS})$ is shown in Fig. 9. Both can use power function fitting, i.e.,

$$V_F(I_F) = g \cdot I_F^h + J \quad (25)$$

$$Q_{rr}(I_{off}, V_{DS}) = k \cdot I_{off}^p + Q \quad (26)$$

where, g, h, J, k, p , and Q are curve-fitting coefficients.

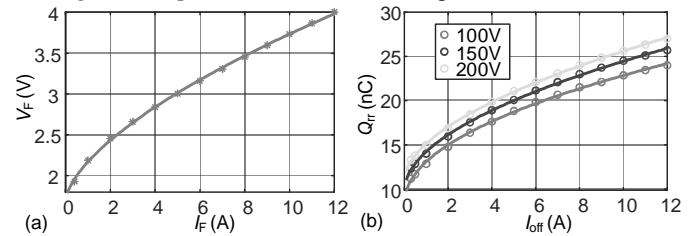


Fig. 9 Curve-fitting for diode forward voltage and reverse recovery charge. (a) $V_F(I_F)$. (b) $Q_{rr}(I_{off}, V_{DS})$.

Hence, the MOSFET body diode loss can be estimated as,

$$P_{diode} = P_{D,con}(S_1, S_2, S_3, S_4) + P_{D,r}(S_1, S_2, S_3, S_4) \quad (27)$$

It is noted that the MOSFET body diode can realize ZCS when the MOSFET achieves ZVS, making the diode reverse recovery loss zero. Combined with (10)-(28), the total loss of the FSBB converter can be expressed as

$$P_{loss}(\delta, d_1, d_2, f_s) = P_{con} + P_{core} + P_{sw} + P_{diode} \quad (28)$$

IV. OPTIMIZATION RESULTS AND PROPOSED CONTROLLER

As FSBB converters can operate in different modulation modes (resulting in different power losses) under the same load condition, an optimization exercise is needed to find the maximum possible power efficiency. In this paper, the GQPSO algorithm is used in conjunction with the established loss model to identify the minimal loss point.

A. Optimization Objective Function and Constraints

The objective function and constraints of the optimization exercise are given in (29). Based on the inductor core frequency characteristics obtained from the datasheet, the switching frequency range is set to 0~1 MHz. The phase angle range is δ 0~1 corresponding to values from 0° to 360°. When the FSBB converter operates in buck mode, the range of the duty cycle d_2 is 0~1, and the duty cycle $d_1 = m d_2$ ($m = V_o / V_{in} \leq 1$, m is voltage gain). Similarly, when the FSBB converter operates in boost mode, the duty cycle d_1 has a range 0~1, and the duty cycle $d_2 = d_1 / m$ ($m > 1$). The target output current I_o is the equality constraint of the objective function. Combining the constraints for d_1, d_2, δ, f_s and I_o , the standard form function for optimization is

$$\begin{aligned} \min P_{\text{loss}}(\delta, d_1, d_2, f_s) &= P_{\text{con}} + P_{\text{core}} + P_{\text{sw}} + P_{\text{diode}} \\ \text{s.t. } I_o &= I_{o,\text{set}} \\ 0 \leq \delta &\leq 1 \text{ (i.e., } 0 \sim 360^\circ) \\ 0 < f_s &\leq 1 \text{ MHz} \\ \text{buck: } 0 \leq d_2 &\leq 1, 0 < m < 1, d_1 = md_2 < 1 \\ \text{boost: } 0 \leq d_1 &\leq 1, 1 < m, d_2 = d_1/m < 1 \end{aligned} \quad (29)$$

where, $I_{o,\text{set}}$ is the expected output current. m is voltage gain, $m = V_o/V_{\text{in}}$. Due to the constraints of the voltage gain, only three control variables need to be optimized.

B. Gaussian Quantum-behaved Particle Swarm Optimization

The particle swarm optimization algorithm is commonly applied to power electronic converter control [21] and mobile edge computing [22] etc. Here, the GQPSO algorithm proposed in [23] is used to search for a minimal power loss. Compared with conventional PSO, GQPSO is not prone to falling into local optima. GQPSO procedure is as follows. The corresponding flow chart is shown in Fig. 10.

Step 1: Generate randomly the initial particle swarm. The initial personal best $pbest$ is equal to the initial particle swarm.

Step 2: Substitute the initial particle swarm into the objective function (29). Then compare each particle's fitness to get the initial global $gbest$.

Step 3: Calculate weighting factor ω through

$$\omega = \omega_{\min} + (\omega_{\max} - \omega_{\min})(\text{iter} - \text{iter}_{\max})/\text{iter}_{\max} \quad (30)$$

where, iter is the number of GQPSO iterations step.

Step 4: Calculate the mean of personal best $Mpbest$.

Step 5: Calculate the local attractor L_a by

$$L_a = (G_1 \cdot pbest + c_2 \cdot G_2 \cdot gbest)/(G_1 + G_2) \quad (31)$$

where, $G_1 = \text{abs}(N(0,1))$, $G_2 = \text{abs}(N(0,1))$, $\text{abs}(N(0,1))$ is random numbers generated using the absolute value of the Gaussian probability distribution with zero mean and unit variance.

Step 6: Update the particle swarm according to

$$\begin{cases} x_i(t+1) = L_a + \omega \cdot |Mpbest - x_i(t)| \cdot \ln(1/G), & \text{if } k \geq 0.5 \\ x_i(t+1) = L_a - \omega \cdot |Mpbest - x_i(t)| \cdot \ln(1/G), & \text{if } k < 0.5 \end{cases} \quad (32)$$

where, $G_1 = \text{abs}(N(0,1))$, k is the value generated using $\text{abs}(N(0,1))$.

Step 7: Substitute the new particle swarm into the objective function (29). Then compare each particle's fitness with the $pbest$ to update $pbest$ with a smaller value.

Step 8: Compare the fitness with the population's overall previous $gbest$ to update $gbest$ with a smaller value.

Step 9: Repeating the evolutionary cycle: Loop to Step 3 until a stop criterion (i.e., iteration number $\text{iter} = \text{iter}_{\max}$) is met.

In this study, $\text{iter}_{\max} = 100$. Under this condition, a single run of the GQPSO algorithm using MATLAB takes about 147.2 seconds. With this, a set of control parameters corresponding to a certain load can be obtained. The proposed algorithm requires a certain level of computational resources to construct an offline look-up table of control parameters with which to implement the controller.

C. Optimization Results

Due to voltage gain constraints ($d_1/d_2 = m = V_o/V_{\text{in}}$), the four control variables can be simplified down to three. From the GQPSO optimization results, the trend of control variables with the output current is shown in Fig. 11 (buck mode) and Fig. 12 (boost mode). It can be seen from Fig. 11(a) that the trend of the

control variables is discontinuous and is clearly divided into three parts, which corresponds to light load, medium load, and heavy load conditions, respectively. Fig. 11 and Fig. 12 show that the switching frequency is low at light load and begins to increase dramatically at medium and heavy loads to reduce the inductor current RMS value. Following this rise, the switching frequency begins to slowly decrease to reduce the switching loss and meet the output current requirement while ensuring that the total loss is minimal. For buck mode operation, the minimal switching frequency is 29.63kHz at 0.4A (10% load) and the maximum switching frequency is 191.57kHz at 1.6A. The minimal switching frequency is 51.59kHz at 0.4A (10% load) and the maximum switching frequency is 185.19kHz at 0.9A for boost mode operation.

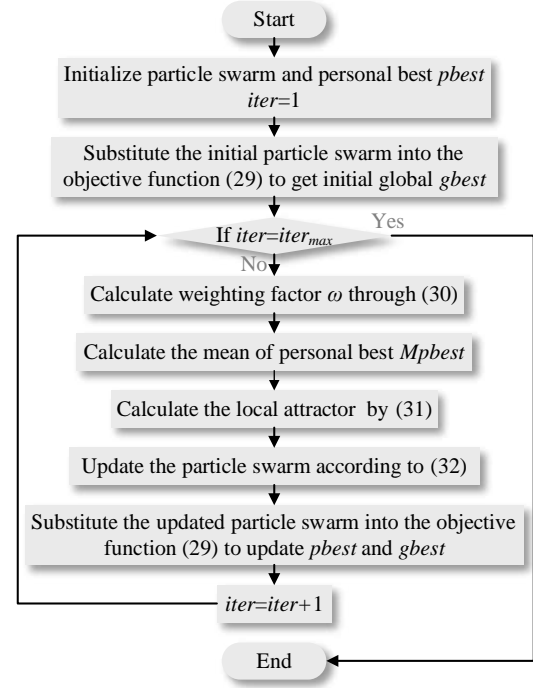


Fig. 10 GQPSO flow chart.

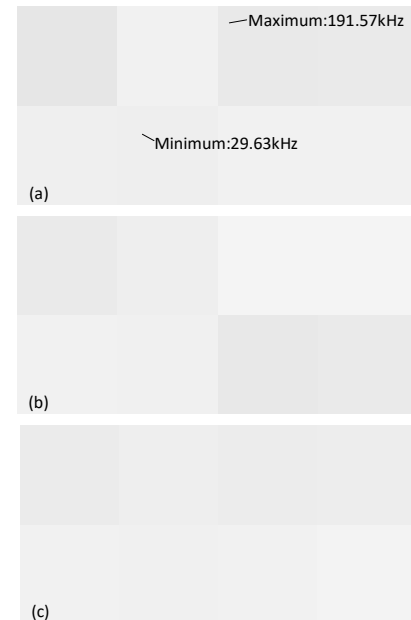


Fig. 11 Control parameters from GQPSO optimization results for buck mode, 600W converter. (a) Switching frequency. (b) Phase angle δ . (c) Duty cycle d_2 .

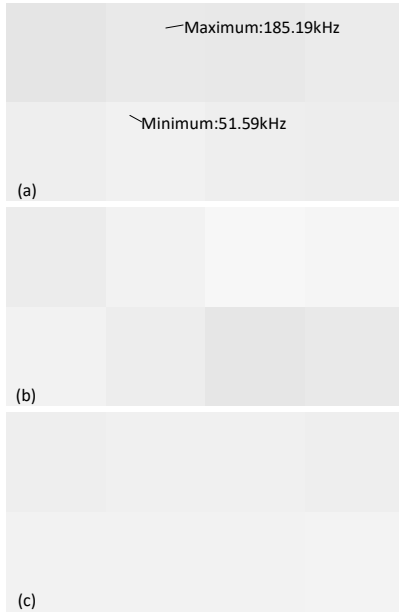


Fig. 12 Control parameters from QGPSO optimization results for boost mode, 600W converter. (a) Switching frequency. (b) Phase angle δ . (c) Duty cycle d_1 .

For load values of 10% and less, the switching frequency is constant (at the 10% value). The upper limit of switching frequency is dependent on optimization results and is very hard to calculate by a given formula. This will be considered in more detail in Section V where the inductor design process is outlined.

The minimum switching frequency is 29.63kHz, well within the normal switching frequency range of a power electronic converter. If needed, an EMI filter can easily be designed for a cut-off frequency of 29.63kHz. This will also meet the filtering requirement when the switching frequency is increased because the EMI filter contains a (equivalent) low pass filter.

The optimization results show that three different modulation modes apply in light load, medium load, and heavy load conditions, respectively. The evolution of loss and control variables with the iteration step, and estimated voltage and current waveforms by frequency-domain expressions are shown in Fig. 13 (buck mode) and Fig. 14 (boost mode). All switches can achieve ZVS in the modulation mode shown in Fig. 13 (b) and Fig. 14 (b). The modulation modes of Fig. 13 (d) and Fig. 14 (d) are similar to that in Fig. 8, and the remaining two switches can achieve ZVS. There is only one switch that can realize ZVS in the modulation mode shown in Fig. 13 (f) and Fig. 14 (f). This is because the minimal value of the inductor current is more than zero, which cannot meet the ZVS requirements. The above conclusions will be verified experimentally in Section VI.

Based on the optimization results, the proposed control block diagram of the FSBB converter is shown in Fig. 15. The QGPSO algorithm is executed for different output currents I_o conditions to develop an offline look-up table for δ , d_1 , d_2 , and f_s . This table is then utilized in the digital signal processing (DSP) controller of the FSBB converter. The output current is filtered by a low pass filter to avoid the possibility of a change in frequency because of measurement noise. The control variable d_1 is controlled via a PI controller to keep the output voltage constant under buck mode, and the remaining control variables are obtained by looking table. Similarly, the control variable d_2 is controlled via a PI controller to keep the output voltage constant under boost mode, and the remaining control variables are obtained by looking table.

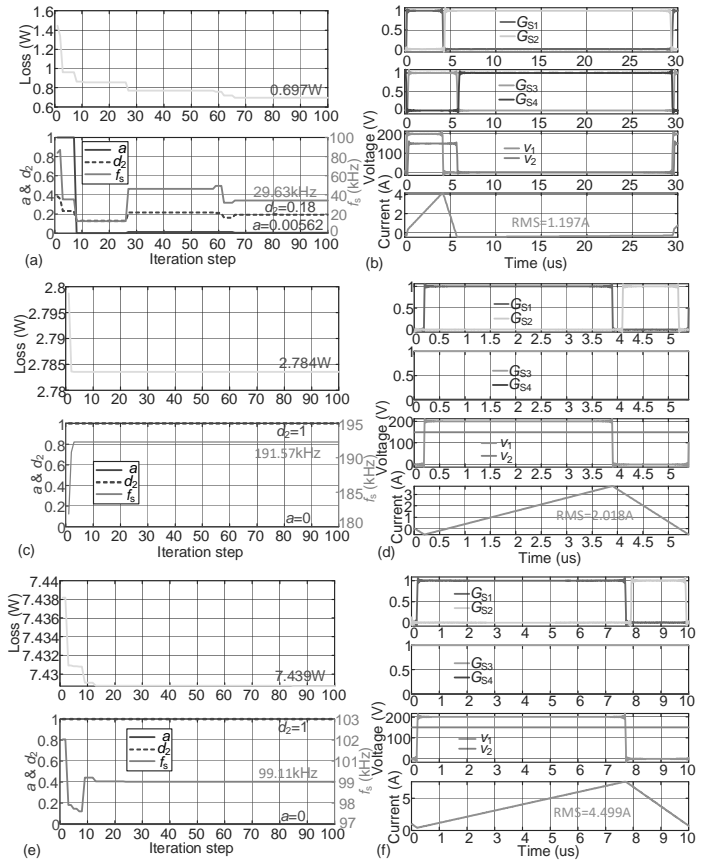


Fig. 13 Three different optimal modulation modes for buck mode, 600W. (a)-(b) with output current of 0.4A. (c)-(d) with output current of 1.6A. (e)-(f) with output current of 4A. (a), (c) & (e) show the evolution of loss and control variables with the iteration step. (b), (d) & (f) illustrate the estimated voltage and current waveforms by frequency-domain expressions.

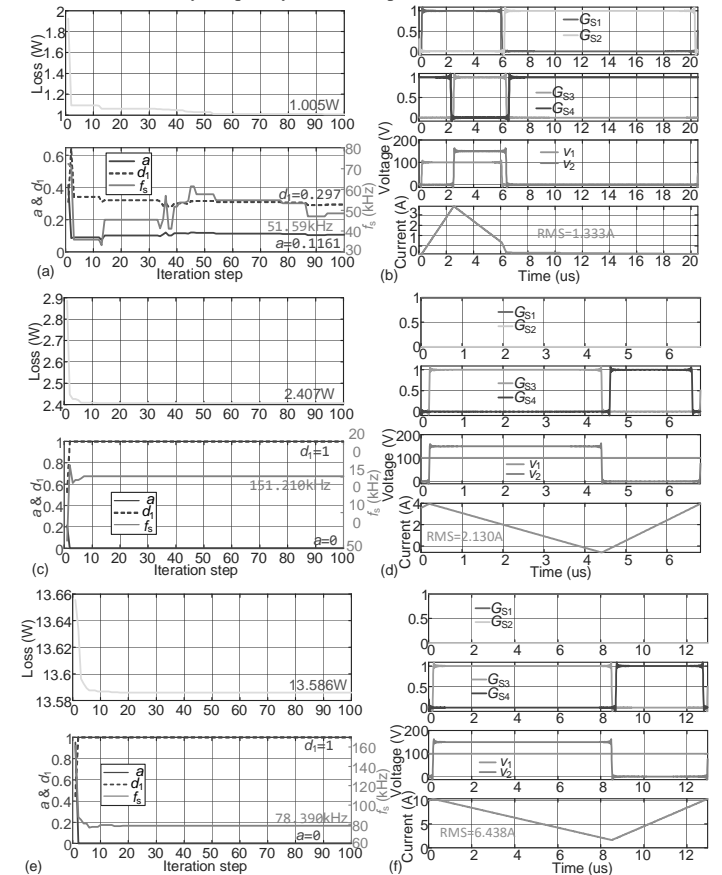


Fig. 14 Three different optimal modulation modes under boost mode, 600W. (a)-(b) with output current of 0.4A. (c)-(d) with output current of 1.6A. (e)-(f) with output current of 4A. (a), (c) & (e) show the evolution of loss and control variables with the iteration step. (b), (d) & (f) illustrate the estimated voltage and current waveforms by frequency-domain expressions.

(b) with output current of 0.4A. (c)-(d) with output current of 1.2A. (e)-(f) with output current of 4A. (a), (c) & (e) show the evolution of loss and control variables with the iteration step. (b), (d) & (f) illustrate the estimated voltage and current waveforms by frequency-domain expressions.

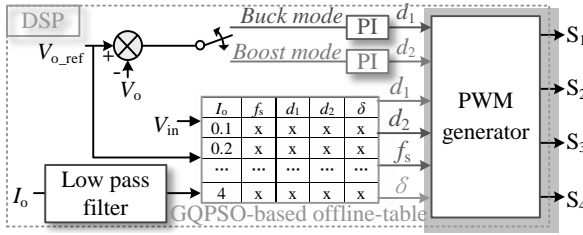


Fig. 15 FSBB control block diagram.

V. FSBB Converter Design Parameters

A. Inductor Value Design

In the traditional buck-boost converter, the inductor value commonly depends on the given ripple current requirement and the given switching frequency. In this study, the switching frequency changes with load conditions. For the determination of the inductance, a preset reference frequency f_{ref} is used. Here, the switching frequency of the converter operating in buck mode at full load will be taken as the preset reference frequency. Based on the analysis of a large number of GQPSO optimization results, the maximum switching frequency of the converter will be around twice the preset reference switching frequency.

A small inductance value is desirable because it means a smaller inductor volume. However, this comes at the cost of a higher current ripple component and thus, care must be taken to ensure that it is kept within acceptable levels. An excessive ripple current will result in a large DC bus capacitance value and an increase in the current stress on the converter switching devices. In this study, the current ripple for buck mode operation was set to be slightly higher than, but less than twice the value of the maximum output current. The optimization results presented in Section IV-C show that the FSBB converter operates in two-switch buck mode (Fig. 8 (b)) under full load. The relationship between the ripple current and inductor value under this operating condition can be expressed as

$$\Delta i_L = (V_1 - V_2) d_1 T_{ref} / L = \frac{m(V_1 - V_2)}{f_{ref} L} \quad (33)$$

where, $T_{ref} = 1/f_{ref}$ is the preset reference switching period. $m = V_o/V_{in}$ is the voltage gain of the FSBB converter.

$$I_{o,max} < \Delta i_L < \beta I_{o,max} \Rightarrow \frac{(V_1 - V_2)m}{\beta f_{ref} I_{o,max}} < L < \frac{(V_1 - V_2)m}{I_{o,max} f_{ref}} \quad (34)$$

where, $\beta = 2$ is a coefficient used to limit the maximum inductor current ripple. In this study, f_{ref} is set to 100kHz. Substituting the relevant parameters given in Table II into (34), values of $46.88\mu H < L < 93.75\mu H$ are obtained. A value of $L = 50.5\mu H$ was used.

Once the value of L is known, it is used by the optimization algorithm to arrive at the optimal result. The peak values of inductor current for minimum losses under different load conditions are recorded and compared to obtain the maximum value used for the selection of the inductor core and the design of the number of turns.

The actual manufactured inductor will inevitably have a small tolerance. However, the proposed control method is robust to inductor tolerance. This is because when the control parameters

remain unchanged and the inductance changes by 1% (which is a relatively large tolerance), the loss changes by only 0.01W. When the inductance remains unchanged, there are many control parameters corresponding to a loss change of 0.01W. Therefore, it can be concluded that the proposed method is highly robust to the tolerance of the inductor.

B. DC Bus Capacitor Value Design

Substituting the relevant optimized control parameters into the circuit simulation model reveals that the capacitor ripple voltage varies the most in boost mode at full load. Under these conditions, the output voltage ripple can be expressed as

$$C \geq \frac{\Delta Q}{\Delta V} = \frac{I_{o,max}(1-d_2)T_{ref}}{\Delta V} = \frac{I_{o,max}(1-1/m)}{\lambda V_2 f_b} \quad (35)$$

where, $\lambda = 1\%$ is the output voltage ripple coefficient. f_b is the switching frequency in boost mode at full load. Substituting the relevant parameters given in Table II into (35), values of $C \geq 113.4\mu F$ are obtained. $C_{in} = C_o = 1000\mu F$ in this paper.

VI. Experiment Results and Discussion

Two laboratory prototypes of the FSBB converter were designed and constructed to verify the operating characteristics of the proposed FSBB converter, one rated at 600W and one at 1500W.

A. Experimental Results at 600W

Fig. 16 shows the developed 600W laboratory prototype of the FSBB converter utilized to verify the proposed loss model and GQPSO optimizing results. It is a left-right symmetrical structure, including left-right symmetrical voltage and current sensors. The prototype parameters are given in Table II.

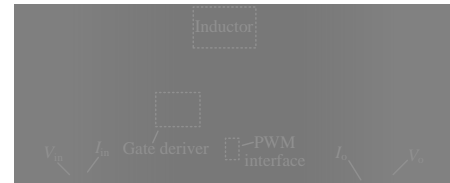


Fig. 16 A laboratory prototype of a 600W FSBB converter.

TABLE II

EXPERIMENTAL PLATFORM PARAMETERS FOR 600W CONVERTER	
Parameters	Values
Rated output current I_o	4A
Input voltage V_{in}	100~200V
Output voltage V_o	150V
Rated power	600W
Inductor L	50.5μH
Switching frequency range in buck mode	29.63kHz~191.57kHz
Switching frequency range in boost mode	51.59kHz~185.19kHz
Inductor core	PQ26/25-N95
MOSFET	SCT3120AL
Dead-time T_D	200ns
Capacitor C_{in} and C_o	1000μF

Experimental voltage and current waveforms of three different optimal modulation modes are shown in Fig. 17 to Fig. 22. Here, Fig. 17 to Fig. 19 show buck mode experimental results that correspond to the estimated results in Fig. 13, and Fig. 20 to Fig. 22 show boost mode experimental results that correspond to the estimated results in Fig. 14. It can be found that estimated voltage and current waveforms are similar to the experimental waveforms. Note that only one switch cannot achieve ZVS when the output current is 4A. In the remaining conditions, these

switches that work at high frequency achieve ZVS, which is consistent with the judgment from Fig. 13 and Fig. 14. In addition, Table III summarizes the estimated and measured inductor current RMS value. The maximum error is 3.5%, which proves the accuracy of frequency-domain expression estimation.

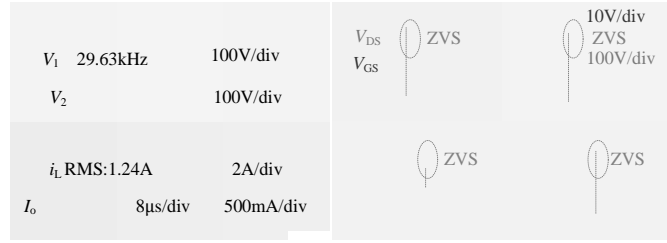


Fig. 17 Buck mode: voltage and current waveforms with 0.4A output current, 600W converter.

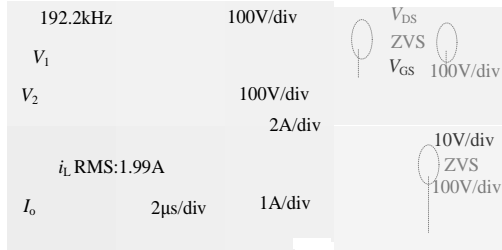


Fig. 18 Buck mode: voltage and current waveforms with 1.6A output current, 600W converter.

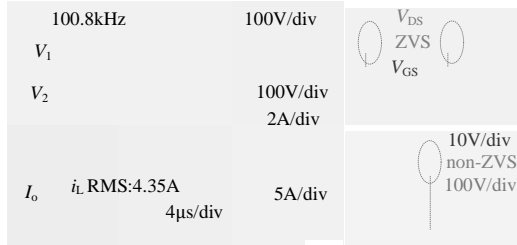


Fig. 19 Buck mode: voltage and current waveforms with 4A output current, 600W converter.

The measured power efficiency curve of the proposed control method is illustrated in Fig. 25. Under buck mode operation, the minimum power efficiency is 98.78%, and the maximum power efficiency is 98.96%. Under boost mode, the minimum power efficiency is 97.79%, and the maximum power efficiency is 98.53%.

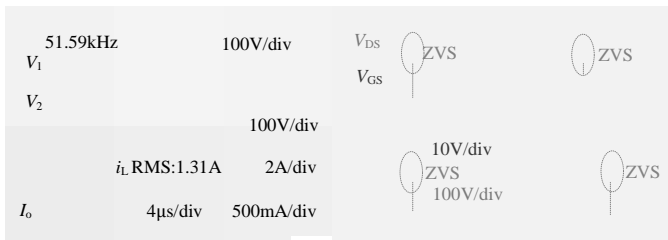


Fig. 20 Boost mode: voltage and current waveforms with 0.4A output current, 600W converter.

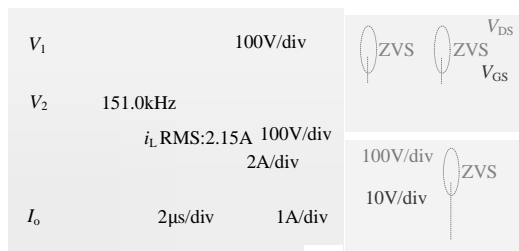


Fig. 21 Boost mode: voltage and current waveforms with 1.2A output current, 600W converter.

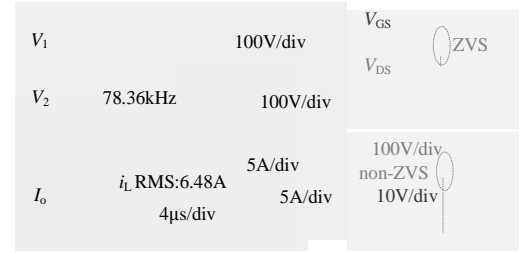


Fig. 22 Boost mode: voltage and current waveforms with 4A output current, 600W converter.

The dynamic characteristics of the proposed controller are shown in Fig. 23 and Fig. 24. The controller can remain stable during load step changes, which illustrates that the proposed controller has sufficient robustness. The process of reducing the inductor current RMS value by increasing the switching frequency when there is a change from light to heavy load conditions can be clearly seen in Fig. 23. The response time of the proposed controller is about 30ms, which is slightly longer than the dynamic response time of existing state-of-the-art methods. The reason for the relatively slower dynamic response of the proposed controller is as follows. To ensure accuracy when selecting data from the look-up table, the measured current passes through a low pass filter to reduce any fluctuations that may affect the accuracy of data selection from the look-up table. In addition, the PI controller is designed with a relatively low bandwidth to reduce fluctuations in the output voltage and current waveforms.

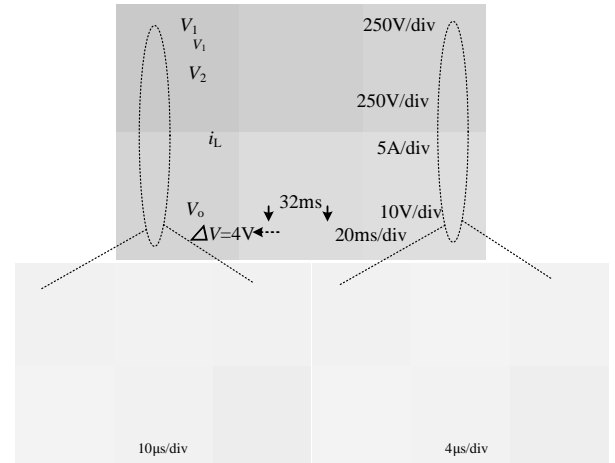


Fig. 23 Load change in buck mode, 600W converter. The output current changes from 0.8A to 1.6A. The process of reducing the inductor current RMS value by increasing the switching frequency can be seen.

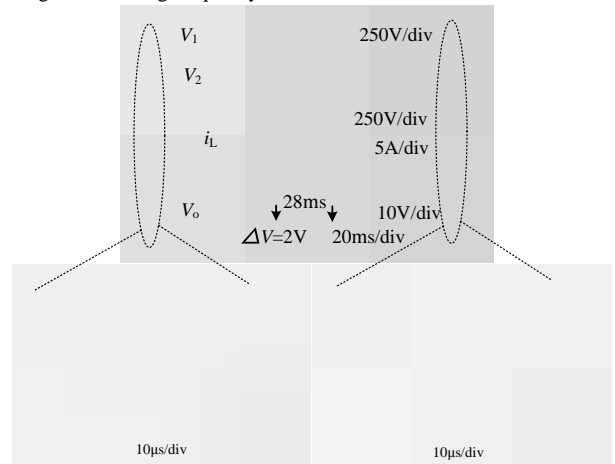


Fig. 24 Load change in boost mode, 600W converter. The output current changes from 1.6A to 0.8A.

TABLE III
DEVIATION BETWEEN ESTIMATE AND MEASUREMENT

	Buck mode			Boost mode		
Estimate	1.197	2.018	4.499	1.333	2.130	6.438
Measurement	1.24	1.99	4.35	1.31	2.15	6.48
Error (%)	3.5%	1.4%	3.3%	1.7%	0.9%	0.6%

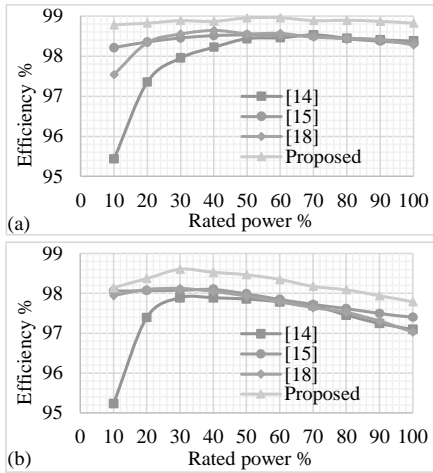


Fig. 25 Measured efficiency comparison between the proposed method and three state-of-the-art three methods, 600W converter. Here, these methods were reproduced in the laboratory prototype of this paper. (a) buck mode, $V_{in}=200V$. (b) boost mode, $V_{in}=100V$.

B. Experimental Results at 1500W

To verify the proposed method at a higher power level, a new laboratory prototype FSBB converter rated at 1500W was constructed (photo shown in Fig. 26). The parameters of the new PCB and 1500W experiment are given in Table IV.



Fig. 26 Laboratory prototype for 1500W power level.

TABLE IV
EXPERIMENTAL PLATFORM PARAMETERS FOR 1500W

Parameters	Values
Rated output current I_o	4.286A
Input voltage V_{in}	300~400V
Output voltage V_o	350V
Rated power	1500W
Inductor L	50.3μH
Switching frequency range in buck mode	17.5kHz~152.1kHz
Switching frequency range in boost mode	23.1kHz~118.5kHz
Inductor core	PQ26/25-N95
MOSFET	SCT3080KLHR
Dead-time T_D	200ns
Capacitor C_{in} and C_o	470μF

Waveforms for 10%, 50%, and 100% load conditions are shown in Fig. 27. It can be seen that the waveform profile of the 1500W rated prototype at 10% load (Fig. 27(a) and Fig. 27(b)) and 50% load condition (Fig. 27(c)) are the same as those of the 600W rated converter. The remaining profiles are different because a new global optimal point is obtained with the 1500W prototype parameters. This can be shown by comparing the efficiency with that obtained with three state-of-the-art methods presented in [14], [15], and [18]. The measured converter power efficiency curves are shown in Fig. 28. It can be seen that the

power efficiency of the proposed converter is higher than that of the three other state-of-the-art methods, achieving maximum efficiency of 99.27% in buck mode and 99.11% in boost mode.



Fig. 27 1500W converter waveforms for 10%, 50%, and 100% load conditions. (a) 10% load in buck mode. (b) 10% load in boost mode. (c) 50% load in buck mode. (d) 50% load in boost mode. (e) 100% load in buck mode. (f) 100% load in boost mode.

C. Comparison and Discussion

To verify the advantages of the proposed methodology, a comparison with three state-of-the-art methods is presented in Table V. The three methods from the literature were reproduced on the proposed experimental prototypes (600W and 1500W) and the efficiency curves were measured and compared.

The following conclusions can be drawn from the comparative analysis of the table contents. Existing state-of-the-art methods focus on minimizing the inductor current RMS value (conduction loss) and neglect the impact of switching losses. In contrast, the proposed method establishes a comprehensive loss model which is then used as an optimization target for finding the minimum loss. Switching losses and core losses are taken fully into account in the optimization process, clearly leading to more accurate results than when considering the reduction in inductor RMS current value and conduction losses only. Another drawback of the existing state-of-the-art methods is that they do not encompass all possible modulation modes in the optimization process, failing to arrive at the global minimum loss. This is reflected in the fact that the efficiency curves of the three methods are significantly lower than the efficiency curve obtained by the proposed method at all load levels. Only the method presented in [14] takes the switching frequency into account in the optimization of the current RMS value. However, the study failed to consider the increase in switching losses resulting from the reduction of the inductor RMS current value obtained by increasing the switching frequency. Whether the total losses increased or decreased under these conditions was

not determined in [14].

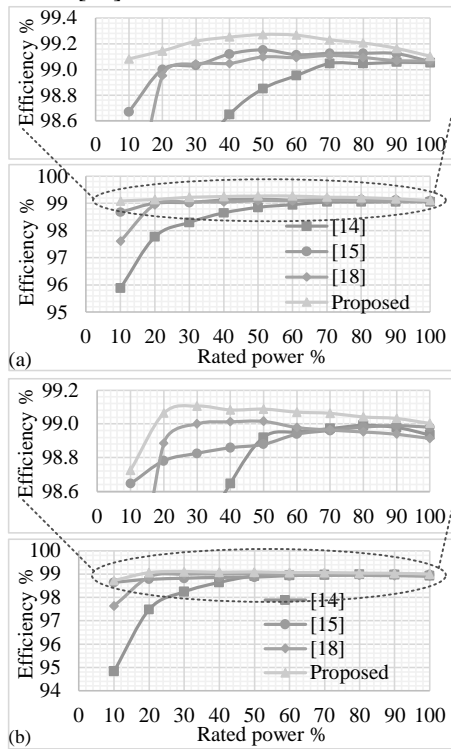


Fig. 28 Measured efficiency comparison between the proposed method and three state-of-the-art three methods, 1500W converter. Here, these methods were reproduced in the laboratory prototype of this paper. (a) buck mode, $V_{in}=400V$. (b) boost mode $V_{in}=300V$. The maximum efficiency is 99.27% in buck mode and 99.11% in boost mode.

TABLE V

COMPARISON WITH THE THREE STATE-OF-THE-ART METHODS

Paper	[14]	[15]	[18]	Proposed
Optimization target	Inductor current RMS value	Inductor current RMS value	Inductor current RMS value	Total loss
Number of optimized modulation modes	1	1	10	All
Global optimum	No	No	No	Yes
Switching frequency	Variable	Constant	Constant	Variable
Light load efficiency	Low	Low	Low	High
Full load efficiency	Low	Low	Low	High

The efficiency curve comparison with the three state-of-the-art methods is shown in Fig. 25 and Fig. 28. It can be seen that the efficiency of the proposed method is higher than that of the existing three state-of-the-art methods over the entire range of load conditions. To analyze the reason for the higher efficiency, a power loss analysis is presented in Fig. 29. Fig. 29(a) shows that the switching loss and conduction loss of the proposed method are lower than those of the existing three state-of-the-art methods. This is because the proposed method uses a lower switching frequency and appropriate duty cycle and phase angle values at 10% load, giving a higher light load efficiency. Fig. 29(b) shows that the switching loss of the proposed method is a little higher than that of the three state-of-the-art methods, while the conduction loss is lower. This is because conduction losses dominate at heavy loads and can be significantly reduced by increasing the switching frequency to reduce the RMS value of the inductor current. Fig. 30 shows the power analysis of 1500W

converter in boost mode at 50% load. The method in [14] reduces the inductor current RMS value (conduction loss) by increasing the switching frequency, as demonstrated in Fig. 30. However, the total loss is higher than that of the proposed method. This is because the trade-off between the switching loss and the conduction loss is not considered in [14].

Based on the above analysis, the following conclusion can be drawn: the trade-off between switching loss and conduction loss must be considered when the switching frequency is added to the efficiency optimization of the FSBB converter to obtain global optimal efficiency.

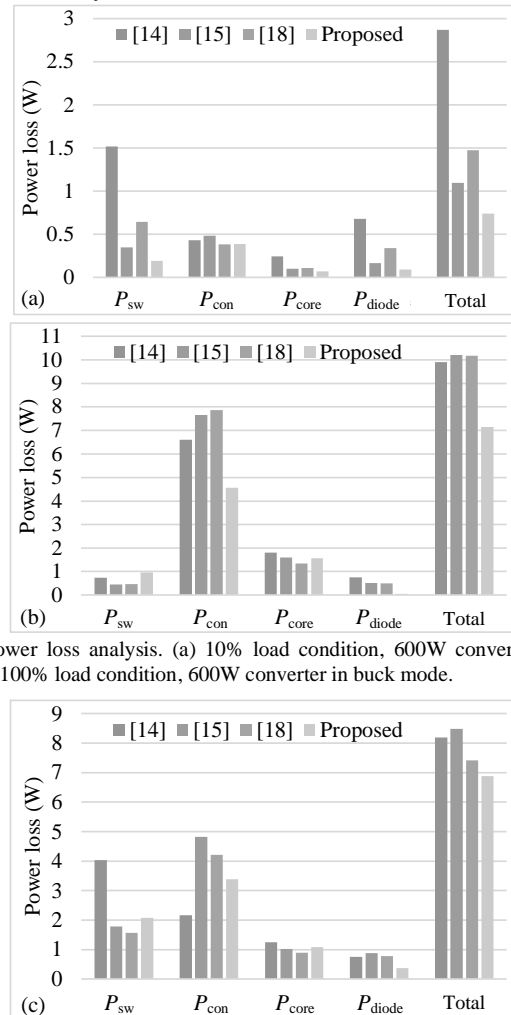


Fig. 29 Power loss analysis. (a) 10% load condition, 600W converter in buck mode. (b) 100% load condition, 600W converter in buck mode.

Fig. 30 Power loss analysis, 50% load condition, 1500W converter in boost mode.

VII. Conclusion

In this paper, a generalized inductor current frequency-domain expression that can represent all possible modulation modes for FSBB is derived. In this case, all possible debugging modes are involved in the optimization to find the global optimum. A loss model for FSBB based on the frequency-domain expressions is established. With the developed model, the switching loss can be estimated based on the drive signal PWM and inductor current frequency-domain expressions. Further, to find the global minimal power loss point, in the proposed work, Gaussian quantum-behaved particle swarm optimization is utilized. The switching frequency is added to the power loss optimization. The trade-off between switching loss and conduction loss is found,

resulting in significant efficiency improvements over previous approaches. The proposed work is validated through analytical and experimental studies achieving a maximum efficiency of 98.96% for the 600W-rated laboratory prototype and 99.27% for the 1500W-rated laboratory prototype.

Appendix

The derivation process of (4) is as follows:

$$\begin{aligned}
 v_L(t) &= V_{in} \cdot G_{S1}(t) - V_o \cdot G_{S3}(t) = v_1(t) - v_2(t) \\
 d'_1 &= d_1 - d_D \\
 d'_2 &= d_2 - d_D \\
 i_{ripple}(t) &= (v_1(t) - v_2(t)) / n\omega L \\
 &= \frac{V_{in}d'_1 - V_o d'_2 + 2V_{in}d'_1 \sum_{n=1}^{\infty} \frac{\sin\left(n\omega \frac{d'_1 T_s}{2}\right)}{n\omega \frac{d'_1 T_s}{2}} \cdot \cos\left(n\omega t - nd'_1\pi - \frac{\pi}{2}\right) - 2V_o d'_2 \sum_{n=1}^{\infty} \frac{\sin\left(n\omega \frac{d'_2 T_s}{2}\right)}{n\omega \frac{d'_2 T_s}{2}} \cdot \cos\left(n\omega t - n\left(d'_2 + 2(a + d_D)\right)\pi - \frac{\pi}{2}\right)}{n\omega L} \\
 &= \frac{V_{in}d'_1 - V_o(d_2 - d_D) + \sum_{n=1}^{\infty} 2V_{in}d'_1 \frac{\sin\left(n\omega \frac{d'_1 T_s}{2}\right)}{n\omega \frac{d'_1 T_s}{2}} \cdot \cos\left(n\omega t - \left(nd'_1\pi + \frac{\pi}{2}\right)\right) - \sum_{n=1}^{\infty} 2V_o(d_2 - d_D) \frac{\sin\left(n\omega \frac{d'_2 T_s}{2}\right)}{n\omega \frac{d'_2 T_s}{2}} \cdot \cos\left(n\omega t - \left(n\left(d'_2 + 2(a + d_D)\right)\pi + \frac{\pi}{2}\right)\right)}{n\omega L} \\
 &= \frac{V_{in}d'_1 - V_o(d_2 - d_D) + \sum_{n=1}^{\infty} 2V_{in}d'_1 \text{sinc}\left(n\omega \frac{d'_1 T_s}{2}\right) \cos(n\omega t) \cos\left(nd'_1\pi + \frac{\pi}{2}\right) + \sum_{n=1}^{\infty} 2V_{in}d'_1 \text{sinc}\left(n\omega \frac{d'_1 T_s}{2}\right) \sin(n\omega t) \sin\left(nd'_1\pi + \frac{\pi}{2}\right) - \sum_{n=1}^{\infty} 2V_o(d_2 - d_D) \text{sinc}\left(n\omega \frac{d'_2 T_s}{2}\right) \cos(n\omega t) \cos\left(n\left(d'_2 + 2(a + d_D)\right)\pi + \frac{\pi}{2}\right) + \sum_{n=1}^{\infty} 2V_o(d_2 - d_D) \text{sinc}\left(n\omega \frac{d'_2 T_s}{2}\right) \sin(n\omega t) \sin\left(n\left(d'_2 + 2(a + d_D)\right)\pi + \frac{\pi}{2}\right)}{n\omega L} \\
 &= \frac{V_{in}d'_1 - V_o d'_2 + \sum_{n=1}^{\infty} 2V_{in}d'_1 \text{sinc}\left(n\omega \frac{d'_1 T_s}{2}\right) \cos\left(nd'_1\pi + \frac{\pi}{2}\right) \cos(n\omega t) + \sum_{n=1}^{\infty} 2V_{in}d'_1 \text{sinc}\left(n\omega \frac{d'_1 T_s}{2}\right) \sin\left(nd'_1\pi + \frac{\pi}{2}\right) \sin(n\omega t) - \sum_{n=1}^{\infty} 2V_o d'_2 \text{sinc}\left(n\omega \frac{d'_2 T_s}{2}\right) \cos\left(n\left(d'_2 + 2(a + d_D)\right)\pi + \frac{\pi}{2}\right) \cos(n\omega t) - \sum_{n=1}^{\infty} 2V_o d'_2 \text{sinc}\left(n\omega \frac{d'_2 T_s}{2}\right) \sin\left(n\left(d'_2 + 2(a + d_D)\right)\pi + \frac{\pi}{2}\right) \sin(n\omega t)}{n\omega L} \\
 &= \sum_{n=1}^{\infty} \left(\frac{V_{in}d'_1 - V_o d'_2}{n\omega L} + \frac{A \sin(n\omega t) + B \cos(n\omega t)}{n\omega L} \right) \\
 &= \sum_{n=1}^{\infty} \frac{V_{in}d'_1 - V_o d'_2}{n\omega L} + \sum_{n=1}^{\infty} \frac{\sqrt{A^2 + B^2}}{n\omega L} \sin\left(n\omega t + \arctan \frac{B}{A}\right)
 \end{aligned}$$

where,

$$\begin{aligned}
 A &= 2V_{in}d'_1 \text{sinc}\left(n\omega \frac{d'_1 T_s}{2}\right) \sin\left(nd'_1\pi + \frac{\pi}{2}\right) - 2V_o d'_2 \text{sinc}\left(n\omega \frac{d'_2 T_s}{2}\right) \sin\left(n\left(d'_2 + 2(a + d_D)\right)\pi + \frac{\pi}{2}\right) \\
 B &= 2V_{in}d'_1 \text{sinc}\left(n\omega \frac{d'_1 T_s}{2}\right) \cos\left(nd'_1\pi + \frac{\pi}{2}\right) - 2V_o d'_2 \text{sinc}\left(n\omega \frac{d'_2 T_s}{2}\right) \cos\left(n\left(d'_2 + 2(a + d_D)\right)\pi + \frac{\pi}{2}\right)
 \end{aligned}$$

The derivation process of (5) is as follows:

$$\begin{aligned}
 i_{ripple}(t) &= \sum_{n=1}^{\infty} \frac{V_{in}d'_1 - V_o d'_2}{n\omega L} + \sum_{n=1}^{\infty} \frac{\sqrt{A^2 + B^2}}{n\omega L} \sin\left(n\omega t + \arctan \frac{B}{A}\right) \\
 i_{ripple,max,n} &= \frac{V_{in}d'_1 - V_o d'_2}{n\omega L} + \frac{\sqrt{A^2 + B^2}}{n\omega L} \\
 I_{ripple,rms} &= \sqrt{\sum_{n=1}^{\infty} \left(\frac{V_{in}d'_1 - V_o d'_2}{n\omega L} \right)^2 + \sum_{n=1}^{\infty} \left(\frac{\sqrt{A^2 + B^2}}{\sqrt{2}n\omega L} \right)^2}
 \end{aligned}$$

References

- [1] U. Sharma and B. Singh, "A Bidirectional Onboard Charger With Multistep Constant Current Charging Capability," in *IEEE Transactions on Transportation Electrification*, vol. 9, no. 1, pp. 1227-1237, March 2023.
- [2] A. Shafiqurrahman, V. Khadkikar and A. K. Rathore, "Vehicle-to-Vehicle (V2V) Power Transfer: Electrical and Communication Developments," in *IEEE Transactions on Transportation Electrification*, 2024, doi: 10.1109/TTE.2023.3345738.
- [3] P. Franzese *et al.*, "Fast DC Charging Infrastructures for Electric Vehicles: Overview of Technologies, Standards, and Challenges," in *IEEE Transactions on Transportation Electrification*, vol. 9, no. 3, pp. 3780-3800, Sept. 2023, doi: 10.1109/TTE.2023.3239224.
- [4] P. Zheng and J. Bauman, "High Efficiency Bidirectional LLC+C Resonant Converter With Parallel Transformers for Solar-Charged Electric Vehicles," in *IEEE Transactions on Transportation Electrification*, vol. 9, no. 1, pp. 1428-1442, March 2023.
- [5] M. -Z. Lu, Z. -W. Guo and C. -M. Liaw, "A Battery/Supercapacitor Hybrid Powered EV SRM Drive and Microgrid Incorporated Operations," in *IEEE Transactions on Transportation Electrification*, vol. 7, no. 4, pp. 2848-2863, Dec. 2021, doi: 10.1109/TTE.2021.3081103.
- [6] G. Lin, J. Liu, C. Rehtanz, C. Li, Y. Li and P. Wang, "Inertia Droop Control and Stability Mechanism Analysis of Energy Storage Systems for DC-Busbar Electric Vehicle Charging Station," in *IEEE Transactions on Transportation Electrification*, vol. 9, no. 1, pp. 266-282, March 2023.
- [7] J. J. Chen, P. N. Shen and Y. S. Hwang, "A High-Efficiency Positive Buck-Boost Converter With Mode-Select Circuit and Feed-Forward Techniques," in *IEEE Transactions on Power Electronics*, vol. 28, no. 9, pp. 4240-4247, Sept. 2013.
- [8] S. Waffler *et al.*, "A Novel Low-Loss Modulation Strategy for High-Power Bidirectional Buck + Boost Converters," in *IEEE Transactions on Power Electronics*, vol. 24, no. 6, pp. 1589-1599, June 2009.
- [9] Z. Zhou, H. Li and X. Wu, "A Constant Frequency ZVS Control System for the Four-Switch Buck-Boost DC-DC Converter With Reduced Inductor Current," in *IEEE Transactions on Power Electronics*, vol. 34, no. 7, pp. 5996-6003, July 2019.
- [10] K. Xia, *et al.*, "Minimising peak current in boundary conduction mode for the four-switch buck-boost DC/DC converter with soft switching," in *IET Power Electronics*, vol. 12, no. 4, pp. 944-954, April, 2019.
- [11] Q. Liu, Q. Qian, M. Zheng, S. Xu, W. Sun and T. Wang, "An Improved Quadrangle Control Method for Four-Switch Buck-Boost Converter With Reduced Loss and Decoupling Strategy," in *IEEE Transactions on Power Electronics*, vol. 36, no. 9, pp. 10827-10841, Sept. 2021.
- [12] L. Tian, X. Wu, C. Jiang and J. Yang, "A Simplified Real-Time Digital Control Scheme for ZVS Four-Switch Buck-Boost With Low Inductor Current," in *IEEE Transactions on Industrial Electronics*, vol. 69, no. 8, pp. 7920-7929, Aug. 2022.
- [13] F. Liu, *et al.*, "A Constant Frequency ZVS Modulation Scheme for Four-Switch Buck-Boost Converter With Wide Input and Output Voltage Ranges and Reduced Inductor Current," in *IEEE Transactions on Industrial Electronics*, vol. 70, no. 5, pp. 4931-4941, May 2023.
- [14] F. Liu, *et al.*, "A Multi-Frequency PCCM ZVS Modulation Scheme for Optimizing Overall Efficiency of Four-Switch Buck-Boost Converter with Wide Input and Output Voltage Ranges," in *IEEE Transactions on Industrial Electronics*, vol. 70, no. 12, pp. 12431-12441, Dec. 2023.
- [15] Z. Guo and T. Mao, "Efficiency Optimization and Control Strategy of Four-Switch Buck-Boost Converter for Wide Conversion Ratio," in *IEEE Transactions on Power Electronics*, vol. 38, no. 9, pp. 10702-10715, Sept. 2023, doi: 10.1109/TPEL.2023.3282203
- [16] X. Ren, *et al.*, "Three-Mode Dual-Frequency Two-Edge Modulation Scheme for Four-Switch Buck-Boost Converter," in *IEEE Transactions on Power Electronics*, vol. 24, no. 2, pp. 499-509, Feb. 2009.
- [17] P. C. Huang, *et al.*, "Hybrid Buck-Boost Feedforward and Reduced Average Inductor Current Techniques in Fast Line Transient and High-Efficiency Buck-Boost Converter," in *IEEE Transactions on Power*

- Electronics*, vol. 25, no. 3, pp. 719-730, March 2010.
- [18] J. Liao, et al., "Lagrange-Multiplier-Based Control Method to Optimize Efficiency for Four-Switch Buck-Boost Converter Over Whole Operating Range," in *IEEE Transactions on Industrial Electronics*, vol. 71, no. 1, pp. 822-833, Jan. 2024.
 - [19] R. Yu, et al., "Computer-Aided Design and Optimization of High-Efficiency LLC Series Resonant Converter," in *IEEE Transactions on Power Electronics*, vol. 27, no. 7, pp. 3243-3256, July 2012.
 - [20] M. A. Montes de Oca, T. Stutzle, M. Birattari and M. Dorigo, "Frankenstein's PSO: A Composite Particle Swarm Optimization Algorithm," in *IEEE Transactions on Evolutionary Computation*, vol. 13, no. 5, pp. 1120-1132, Oct. 2009.
 - [21] Y. Jiang, X. Li, C. Qin, X. Xing and Z. Chen, "Improved Particle Swarm Optimization Based Selective Harmonic Elimination and Neutral Point Balance Control for Three-Level Inverter in Low-Voltage Ride-Through Operation," in *IEEE Transactions on Industrial Informatics*, vol. 18, no. 1, pp. 642-652, Jan. 2022.
 - [22] S. Dong, Y. Xia and J. Kamruzzaman, "Quantum Particle Swarm Optimization for Task Offloading in Mobile Edge Computing," in *IEEE Transactions on Industrial Informatics*, vol. 19, no. 8, pp. 9113-9122, Aug. 2023, doi: 10.1109/TII.2022.3225313.
 - [23] Leandro dos Santos Coelho, "Gaussian quantum-behaved particle swarm optimization approaches for constrained engineering design problems," in *Expert Systems with Applications*, vol. 37, no. 2, pp. 1676-1683, Mar. 2010.

Guanqun Qiu (Student Member, IEEE) received his B.S. degree in electrical engineering from East China Jiaotong University, Jiangxi, China, in 2018, and M.S. degree in electrical engineering from Chongqing University, Chongqing, China, in 2021. He is currently pursuing his Ph.D. degree at Khalifa University, Abu Dhabi, United Arab Emirates. His research interests include DC-DC converters, onboard charger, DC Microgrid, power converters based on SiC and SiC device reliability.

Vinod Khadkikar (Fellow, IEEE) received the M.Tech. degree in power electronics, electrical machines, and drives from the Indian Institute of Technology, New Delhi, India, in 2002 and the Ph.D. degree in electrical engineering from the Ecole de Technologie Supérieure, Montreal, QC, Canada, in 2008. From 2008 to 2010, he was a Postdoctoral Fellow with the University of Western Ontario, London, ON, Canada. In 2010, he was a Visiting Professor with the Massachusetts Institute of Technology, Cambridge, MA, USA. He is currently a Professor with the Department of Electrical Engineering and Computer Science, Khalifa University, Abu Dhabi, United Arab Emirates. His research interests include applications of power electronics in distribution systems and renewable energy resources, grid interconnection issues, power quality enhancement, active power filters, and electric vehicles. Dr. Khadkikar is a distinguished Lecturer of IEEE Industry Applications Society. He is currently Co-EiC of the IEEE Transactions on Industrial Electronics and an Associate Editor for IEEE Transactions on Industry Applications and IET Power Electronics.

Bashar Zahaw (Senior Member, IEEE) received the B.Sc. and Ph.D. degrees in electrical and electronic engineering from Newcastle University, Newcastle upon Tyne, U.K., in 1983 and 1988, respectively. From 1988 to 1993, he was a Design Engineer with a U.K. manufacturer of large variable speed drives and other power conversion equipment. He was appointed as a Lecturer of electrical engineering at The University of Manchester, Manchester, U.K., in 1994. He was a Senior Lecturer at the School of Electrical and Electronic Engineering, Newcastle University, from 2003 to 2014. Since 2014, he has been with the Department of Electrical and Computer Engineering, Khalifa University, Abu Dhabi, United Arab Emirates, where he is currently a Professor of electrical power engineering. His research interests include power conversion, renewable energy, and the application of nonlinear dynamical methods to electrical circuits and systems. Dr. Zahawi was a recipient of the Crompton Premium awarded by the Institution of Electrical Engineers, U.K., and the Denny Medal awarded by the Institute of Marine Engineering, Science and Technology (IMarEST). He was the Chairperson of the IEEE Power and Energy Society, United Arab Emirates Chapter.

Jianquan Liao (Member, IEEE) was born in Fujian, China. He received the B.S. degree in electrical engineering from China University of Petroleum, Qingdao, China, in 2017. He received the Ph.D. degree at Chongqing University, Chongqing, China, in 2021. He is an Associate Research Fellow at the School of Electrical Engineering, Sichuan University, Chengdu, China, since 2021. From September 2019 to September 2020, he is a Guest Researcher of the Delft University of Technology, Delft, Netherlands. He worked in DC Systems, Energy Conversion and Storage Group in Electrical Sustainable Energy, Delft, Netherlands. His research interests include power system protection and control, power quality of the DC distribution network, power system stability and control.